Title

Bijel-templated implantable biomaterials for enhancing tissue integration and vascularization

Permalink

https://escholarship.org/uc/item/0vp602kw

Authors

Thorson, Todd J
Gurlin, Rachel E
Botvinick, Elliot L
et al.

Publication Date

2019-08-01

DOI

10.1016/j.actbio.2019.06.031

Peer reviewed

Published in final edited form as:
Acta Biomater. 2019 August ; 94: 173–182. doi:10.1016/j.actbio.2019.06.031.

Bijel-templated implantable biomaterials for enhancing tissue integration and vascularization

Todd J. Thorson[a], **Rachel E. Gurlin**[b], **Elliot L. Botvinick**[b,c,d,e,*], **Ali Mohraz**[a,f,*]

[a]Department of Chemical and Biomolecular Engineering, University of California, Irvine, CA 92697, USA

[b]Department of Biomedical Engineering, University of California, Irvine, CA 92697, USA

[c]Department of Surgery, University of California, Irvine, CA 92697, USA

[d]Beckman Laser Institute, University of California, Irvine, CA 92697, USA

[e]Edwards Lifesciences Center for Advanced Cardiovascular Technology, University of California, Irvine, CA 92697, USA

[f]Department of Materials Science and Engineering, University of California, Irvine, CA 92697, USA

Abstract

Mitigation of the foreign body response (FBR) and successful tissue integration are essential to ensuring the longevity of implanted devices and biomaterials. The use of porous materials and coatings has been shown to have an impact, as the textured surfaces can mediate macrophage interactions with the implant and influence the FBR, and the pores can provide space for vascularization and tissue integration. In this study, we use a new class of implantable porous biomaterials templated from bicontinuous interfacially jammed emulsion gels (bijels), which offer a fully percolating, non-constricting porous network with a uniform pore diameter on the order of tens of micrometers, and surfaces with consistent curvature. We demonstrate that these unique morphological features, inherent to bijel-templated materials (BTMs), can enhance tissue integration and vascularization, and reduce the FBR. Cylindrical polyethylene glycol diacrylate (PEGDA) BTMs, along with PEGDA particle-templated materials (PTMs), and non-templated materials (NTMs), were implanted into the subcutaneous space of athymic nude mice. After 28 days, implants were retrieved and analyzed via histological techniques. Within BTMs, blood

---

[*]Corresponding Authors: elliot.botvinick@uci.edu, Fax: 949-824-8413 USA, 2416 Engineering Hall, Irvine, CA 92697, mohraz@uci.edu, Fax: 949-824-2541 USA, 916 Engineering Tower, Irvine, CA 92697.

Disclosures
The authors declare no conflicts of interest related to this study.

Data Availability
The raw data required to reproduce these findings are available to download from http://dx.doi.org/10.17632/bms5txwp2h.2 and http://dx.doi.org/10.17632/5f38n5xfjx.2. The processed data required to reproduce these findings are available to download from http://dx.doi.org/10.17632/hgssh35z5k.5 and http://dx.doi.org/10.17632/n9bcksssfj.2.

vessels of increased size and depth, changes in collagen deposition, and increased presence of pro-healing macrophages were observed compared to that of PTM and NTM implants. Bijel templating offers a new route to biomaterials that can improve the function and longevity of implantable devices.

Graphical Abstract

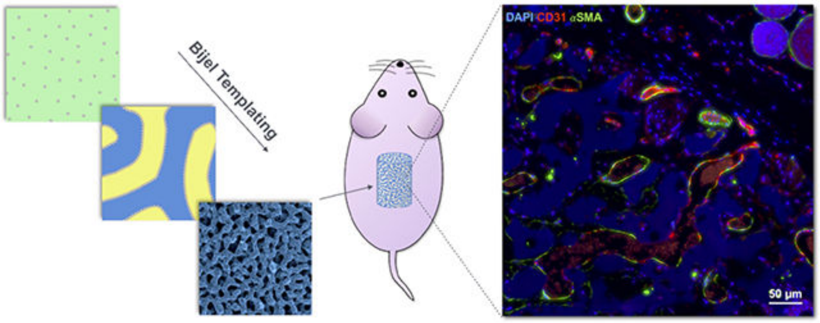

Keywords

bijel; microstructure; foreign body response; porous implants; vascularization

---

1. Introduction

Biomaterials have found widespread use in tissue regeneration, prosthetics, and implantable devices. Their functional lifetime in these applications is largely contingent on the body’s ability to integrate or reject a foreign object. The biological process of implant rejection – or the foreign body response (FBR) – has been, and continues to be, studied extensively [1,2]. Following an implantation event, local tissue damage initiates the body’s normal wound healing process. Blood proteins and platelets may adsorb to the implant surface leading to an inflammatory cascade of neutrophil investigation and macrophage recruitment, frustrated phagocytosis, formation of multi-nucleated foreign body giant cells (FBGCs), and implant failure as the result of collagen encapsulation [3]. Through FBR studies [4,5], a number of controllable factors have been identified that have led to an enriched understanding of tissue integration tools in the design of long-lasting biomaterials.

First, implant surface chemistry dictates immediate protein adsorption and subsequent cell adhesion as hydrophobic surfaces can lead to protein unfolding and irreversible adsorption [6]. Hydrophilic surfaces can decrease, but do not eliminate, protein adsorption [7]. Polyethylene glycol (PEG), a hydrophilic polymer with long-range repulsion of proteins through tight complexing with water molecules [8], is a commonly investigated material to mitigate the FBR to implants [9,10]. Additionally, zwitterionic surfaces formed with materials such as carboxybetaine methacrylate [11], polyampholytes [12], and poly(N-vinylpyrrolidone) (PVPON) [13] have been exploited as biomaterial coatings that provide a neutrally charged surface with minimal protein adsorption. An additional approach to controlling the FBR is achieved through attaching cell receptor ligands to the material to decrease inflammation and increase normal tissue healing around implants [14]. Bioactive signals, such as cluster of differentiation 200 (CD200) [15] and cluster of differentiation 47 (CD47) [16], reduce macrophage infiltration and resist inflammatory cell attachment, respectively. In this approach, the implant is not required to be anti-protein fouling as the ligands interact with responding immune cells.

Second, implant morphology has been intimately linked to FBR mitigation and tissue integration. For example, microscale features at the implant-tissue interface, independent of material composition, have been shown to inhibit collagen remodeling, in turn disrupting the formation of dense, thick fibrosis that would encapsulate the implant [17]. Materials with controlled local curvature or grooved surfaces have also been implicated in the differentiation of immune cells and the FBR [18,19], while sharp edges and acute angles have previously been shown to promote inflammation [20,21]. In addition to surface microfeatures, the presence of an interconnected pore network within the material can provide a route to vascularization and tissue integration [22,23]. The presence of vascular networks within an implant indicates a more natural incorporation of the foreign material and is essential for proper biological function of engineered tissues and devices [24]. For instance, vascularization of implantable biomaterials is particularly important for bio-interfacing devices requiring nutrient and waste shuttling to support implanted tissue such as pancreatic islets [25].

A number of routes exist for imparting porosity to polymeric biomaterials including particle-templating [26], salt leaching [24], gas-foaming [27], electrospinning [28], cryo-gelation [29], and emulsion polymerization [30]. These methods can create pore networks with high degrees of interconnectivity; however, narrow connections (tunnels or windows) between void pockets may disrupt cell migration and full utilization of the void space, and random structures with sharp edges or flat surfaces may increase the FBR as discussed above. Bicontinuous interfacially jammed emulsion gels (bijels) offer a new platform for synthesizing biomaterials with a fully interpenetrating, non-constricting pore network and uniform negative Gaussian curvature (the product of two principle curvatures) along their internal surfaces. Bijels, first proposed in computer simulations by Cates et al. in 2005 [31] and demonstrated experimentally by Herzig et al. in 2007 [32], are unique soft materials that form as the result of kinetic arrest of partially miscible fluids undergoing spinodal decomposition. Upon quenching of a suspension comprised of a critical-composition binary fluid mixture and near-neutral wetting nanoparticles (Fig. 1a) to unstable thermodynamic conditions via a rapid temperature ramp, the nanoparticles adsorb to the newly formed liquid-liquid interface (Fig. 1b) and eventually halt the coarsening process once the interface becomes fully occupied by nanoparticles (Fig. 1c), a jamming transition bearing mechanical signatures of a sharp gelation phenomenon [33,34]. Owing to the dynamics of spinodal decomposition, the resulting bijel comprises bicontinuous, fully percolating fluid domains separated by a nanoparticle monolayer exhibiting negative Gaussian and zero mean curvatures, akin to a perfect saddle, at every point along the jammed interface [35,36]. Following previously reported protocols [33,36], one of the fluid phases is selectively photopolymerized, resulting in a porous polymer scaffold with the morphological characteristics of its parent bijel. Bijel processing has previously been used for the synthesis of three-dimensional (3D) composite electrodes [37], hierarchically porous gold [38] and silver [39] monoliths, cell delivery composites [40], and separation fibers [41,42].

Herein, we explore the use of bijels for developing a new class of implantable biomaterials we term bijel-templated materials (BTMs) with increased tissue infiltration and FBR mitigation potential. Bijel-templated polyethylene glycol diacrylate (PEGDA) implants were processed and implanted subcutaneously in nude mice for 28 days and analyzed with histology and immunohistochemistry. BTM implants were compared to particle-templated material (PTM) and non-templated material (NTM) implants made of PEGDA in the same mice to determine the effect of pore network morphology on tissue infiltration and FBR mitigation.

2. Methods

2.1. Preparation of Study Implants

2.1.1. Bijel-Templated Material Implants—Fluorescently labeled silica nanoparticles (~500 nm) were synthesized following a modified Stöber process [40,43]. Rhodamine B (Sigma-Aldrich) conjugated (3-aminopropyl) triethoxysilane (APTES, TCI America) was mixed overnight with tetraethyl orthosilicate (TEOS, Sigma-Aldrich) in ethanol and strong ammonium hydroxide solution (Fisher Chemical). The synthesized particles were then transferred to 50 mL conical tubes (polypropylene, Greiner), washed by centrifugation (VWR Clinical 200, 2500 rpm, 12 min) and resuspension in deionized water (three cycles), and dried under vacuum (−25 inHg) at 135 °C. Particles were dried under vacuum to tune surface chemistry until they reached near-neutral wetting behavior with respect to a Milli-Q water-rich phase (Millipore, 18.2 MΩ cm at 25 °C) and a 2,6-lutidine-rich phase (Sigma-Aldrich) [44]. Such behavior occurs at a three-phase contact angle $\theta \approx 90°$, resulting in zero net curvature at the water/2,6-lutidine interface [45,46]. The fluorescent labeling of particles allows visualization of bijel formation using confocal microscopy while also contributing to their near-neutral wetting behavior. Bijels were formed by first dispersing particles (1.5% v/v) in Milli-Q water using an ultrasonic horn (Bronson Sonifier 250, Emerson). The resulting dispersion was mixed with 2,6-lutidine (mole fraction of 2,6-lutidine, $x_{lut} = 0.064$), placed in a glass cylinder tube (Simax, Mountain Glass Arts, 5 mm inner diameter) attached to a glass coverslip (No. 1, VWR) using polydimethylsiloxane (Sylgard® 186, Dow Corning), and microwaved for 30 s to initiate phase separation and subsequent bijel formation. The vessel was capped with aluminum foil to prevent evaporation and placed in an oven at 70 °C for 5 min. A hydrogel precursor solution of polyethylene glycol diacrylate (PEGDA; number average molecular weight M_n: 258 g mol^{-1}, Sigma-Aldrich) and 2-hydroxy-2-methylpropiophenone photoinitiator (Darocur® 1173, 1% v/v, Ciba Specialty Chemicals) was gently pipetted on the top surface of the bijel. The cylinder was re-capped and returned to the oven for 4 hr to allow complete transport of the precursor solution into the bijel’s 2,6-lutidine-rich phase to a final precursor concentration of 36.2% v/v. Radical photopolymerization was then performed to selectively polymerize the corresponding monomer-containing domains and form a microporous PEGDA sample using ultraviolet (UV) light (100 W cm^{-2}, wavelength: 320–390 nm, exposure time: 2 min, Lumen Dynamics). Each BTM implant (3 mm diameter) was cut to a length of 3.5 mm and rinsed three times in isopropyl alcohol to remove the remaining liquids and unreacted precursor reagents. Silica nanoparticles were removed from the samples via hydrofluoric acid (HF, Fisher) etching overnight at room temperature. Rhodamine B liberated during silica etching was removed via UV-induced degradation using 1 mg mL^{-1} potassium persulfate (Sigma-Aldrich) in Milli-Q water following the procedure outlined in Chen *et al.* [47]. The potassium persulfate solution was replaced every 10 min (six total cycles).

2.1.2. Particle-Templated Material Implants—

A packed bed of poly(methyl methacrylate) particles (PMMA, diameter: 32–38 μm, Cospheric) was fused in the assembled glass cylinders at 180 °C for 1 hr. Samples were cooled at room temperature for an additional hour, then infiltrated with a solution of PEGDA (36.2% v/v, 1% v/v Darocur® 1173 relative to PEGDA) in 2,6-lutidine and photopolymerization was performed as described above. The resulting PEGDA-PMMA cylinders (3 mm diameter) were submerged in ethyl acetate (Fisher) overnight to remove the PMMA particles, and each resulting PTM implant was cut to a length of 3.5 mm.

2.1.3. Non-Templated Material Implants—

PEGDA (36.2% v/v, 1% v/v Darocur® 1173 relative to PEGDA) in 2,6-lutidine was placed in the assembled glass cylinders and photopolymerization was performed as described above. Each NTM implant (3 mm diameter, 3.5 mm length) was soaked in deionized water overnight at 4 °C to remove 2,6-lutidine.

2.1.4. Implant Sterilization—

All implant samples were rinsed thoroughly with water and dried overnight in a sterile biosafety cabinet at room temperature. Dry samples were sterilized by three 30-min incubations in 70% ethanol, then rinsed three times in sterile phosphate buffered saline (PBS, Gibco), and dried overnight in a sterile biosafety cabinet at room temperature. Samples were then placed in sterilization pouches and autoclaved (Steris SV-120) at 122 °C for 20 min.

2.2. Implant Morphology Characterization

Scanning electron microscopy (SEM) was performed on dry implant samples to characterize the pore network morphology. Samples were sputter-coated with 6 nm of iridium to reduce charging, and micrographs were acquired using a Quanta 3D FEG Dual Beam Microscope (FEI) with an excitation voltage of 10 kV at a 10 mm working distance.

2.3. Implantation

All procedures were approved by the UC Irvine Institutional Animal Care and Use Committee (IACUC #2008–2850) in a facility accredited by the Association for the Assessment and Accreditation of Laboratory Animal Care (AAALAC). Athymic nude mice (Charles River Laboratories) approximately 8-weeks old weighing between 20 and 25 g were selected for this study to analyze the polarization of macrophages, cells critical to the FBR [48], in response to implant morphology. Animals were anesthetized with 2% – 4% isoflurane for surgical experiments. Four small incisions, one in each quadrant of the back of the animal, less than one cm in length through the dorsal skin, were created via sterile surgical scissors. Subcutaneous pockets were created by blunt dissection. Scaffolds were briefly hydrated with sterile saline prior to implantation. A single scaffold was placed within each pocket to prevent movement and potential overlapping of materials during the 4-week study. Implants were placed on their curved edge with the long axis oriented parallel to the spine between the top skin layer and underlying fascia. In other words, the circular flat surfaces of the cylinders were perpendicular to the skin. The dorsal incisions were closed with surgical clips (Fine Science Tools). The animals received ibuprofen, between 50 and 80 mg kg^{-1}, via drinking water for 2 days following surgery. Animals were monitored daily and surgical clips were removed after 14 days. After 28 days, scaffolds and skin samples that received a sham incision were removed and fixed in 4% phosphate-buffered formalin and animals were sacrificed.

2.4. Tissue Processing and Immunohistochemistry

All tissue samples were sent to JIT Labs (Irvine, CA, USA) for processing in paraffin, 4 μm sectioning, and staining with hematoxylin and eosin (H&E) and Masson's Trichrome (MT). Slides were imaged with a Nikon eclipse E800 microscope under 20x magnification (NA: 0.5) using the Olympus "cellSens Entry" program. Images in adjacent fields of view were stitched together using Fiji software [49,50].

2.4.1. Vessel Immunohistochemistry—Following previously described methods [51], tissue sections were deparaffinized with xylene followed by antigen retrieval via overnight incubation in 0.1 M Tris/HCl buffer, pH 9 at 80 °C. Sections were then washed with PBS, permeabilized with 0.5% Triton X-100 (Arcos Organics) and blocked with 5% Donkey serum (Jackson ImmunoResearch) for 60 min at room temperature. After serum blocking, slides were incubated with 0.5% monoclonal rabbit anti-alpha smooth muscle actin (αSMA, Abcam) for labeling pericytes and 0.5% goat anti-cluster of differentiation 31 (CD31, Santa Cruz Biotechnology) for labeling vessel endothelial cells in PBS supplemented with 5% donkey serum and 0.5% Triton X-100 at 4 °C overnight. Slides were then washed with PBS and incubated with 0.2% AlexaFluor488 donkey anti-rabbit (Life Technologies) and 0.25% AlexaFluor594 donkey anti-goat (Jackson ImmunoResearch) in PBS for 1 h. Counter staining for cell nuclei was performed by incubating slides with 0.03% 4',6-diamidino-2-phenylindole, dihydrochloride (DAPI, Invitrogen) for 10 min.

2.4.2. Macrophage Immunohistochemistry—Antigen retrieval was performed by incubating tissue sections in a citrate solution, pH 6 (Dako) in a steam cooker (Black&Decker) for 30 min. Tissue sections were permeabilized and blocked as described above. Slides were then incubated with 1% monoclonal rat anti-F4/80 (BM8, eBioscience) for labeling of all macrophage types [52,53], and 1% polyclonal goat anti-cluster of differentiation 206 (CD206, R&D Systems) for labeling of alternatively activated "M2" macrophages [9,54] in PBS supplemented with 5% Donkey serum and 0.5% Triton X-100 at 4 °C overnight. Slides were washed with PBS and incubated with 0.25% AlexaFluor488 donkey anti-rat (Life Technologies) and 0.25% AlexaFluor594 donkey anti-goat (Jackson ImmunoResearch). Counter staining for cell nuclei was performed by incubating all slides with 0.03% DAPI (Invitrogen) for 10 min.

2.5. Vessel Quantification

Fluorescence microscopy was performed on processed tissue slides labeled for αSMA and CD31 using an Olympus IX83 microscope under 20x magnification (NA: 0.45) using an Orca R2 camera (Hamamatsu Photonics K.K.) and Micro-Manager [55]. Images were acquired for the full BTM and PTM samples in a single section, and a composite image was created by image stitching in Fiji. CD31+ vessel boundaries were traced by hand and used to calculate vessel area and centroid distance to the nearest implant boundary using custom scripts written in MATLAB (MathWorks). Only vessels that resided wholly within the template material were counted.

2.6. Macrophage Quantification

Laser scanning confocal microscopy was performed on processed tissue slides labeled for F4/80 and CD206 using an Olympus IX81 inverted microscope under 40x magnification (NA: 0.6) equipped with a FluoView 1200 laser scanning system and software. Laser wavelengths (λs) of 405 nm, 488 nm, and 559 nm were used to excite DAPI (cell nucleus), AlexaFluor488 (F4/80 macrophage marker label), and AlexaFluor594 (CD206 pro-healing macrophage marker), respectively. Fluorescent emissions from the three fluorophores were detected separately using photomultiplier tubes (PMTs). Specifically, a first dichroic (maximum λ: 490 nm) and barrier filter (λ: 430 – 470 nm) reflected and filtered DAPI emissions for detection in PMT 1. A second dichroic (maximum λ: 560 nm) and barrier filter (λ: 505 – 540 nm) reflected and filtered AlexaFluor488 emissions for detection in PMT 2. Lastly, a mirror and barrier filter (575 – 675 nm) reflected and filtered the remaining AlexaFluor594 emissions for detection in PMT 3. F4/80+ and CD206+ cells were counted in images acquired along the implant interface (0 – 300 μm deep from the interface) using Fiji's cell counter plugin and the percentage of F4/80+ cells also positive for CD206 was calculated. Seven images per implant type per mouse were processed for macrophage quantification.

2.7. Second Harmonic Generation

Second harmonic generation (SHG) imaging was performed on non-labeled tissue sections for a qualitative view of collagen deposition. An inverted Zeiss LSM-780 multi-photon confocal microscope was used for SHG imaging. To increase the efficiency of SHG photon detection, a mirror was placed on top of the tissue slide to back-reflect the forward-scattered light.

2.8. Statistical Analysis

All statistical tests were performed in OriginPro (OriginLab) with $p < 0.05$ considered a statistically significant difference between implant types. Two sample t-tests for individual mouse data and a matched paired t-test for the combined data were used to compare macrophage phenotype differences by implant type. The two sample Kolmogorov-Smirnov test was used to compare vessel area by implant type, because data were typically not normally distributed (Shapiro-Wilk test, $p < 0.05$). Total vessel area per mouse data are presented as mean ± standard error of the mean.

3. Results

3.1. Implant Morphology

Representative SEM micrographs of study implants are shown in Figure 2. The micrograph of the BTM implant (Fig. 2a) suggests that morphological features unique to bijels, including a fully interpenetrating, non-constricting pore network and a polymer surface with relatively uniform, negative Gaussian curvature, are passed on to the sample from its parent template. The PTM implant (Fig. 2b) displayed spherical pores, connected via smaller pore windows (appearing as dark circles) as a result of the partial fusing of the template particles. A superimposed red circle with a diameter of 32 μm is shown in Figures 2a and 2b to demonstrate matching pore sizes between the two templated implants. The solid, NTM implant (Fig. 2c) did not display a porous morphology, as expected. Digital images of representative implant samples are included in Supplementary Data (S1).

3.2. Histology and SHG

Representative images of tissue section slides processed with H&E and MT for histology and SHG are shown in Figure 3. Cellular infiltrate, identified by hematoxylin-stained cell nuclei (violet), was observed deep (>500 μm from the implant-tissue boundary) in the porous implant materials (Fig. 3a, 3b). Infiltrate is present throughout the entire pore network in the BTM implant. Conversely, no infiltrate was present in several areas of the PTM pore network. No infiltrate was observed for the solid, NTM sample. Blood vessels were present in both porous samples (Figures 3a and 3b, filled arrows). Blood vessels were observed spanning the entire pore diameter in the BTM sample, while the vessels within the PTM sample were noticeably thinner. Collagen (Figure 3, open arrows) at the implant-tissue interface was oriented parallel to the interface of PTM and NTM implants, a feature not observed in the BTM samples. Further, a diffuse collagen network was observed within the BTM pores as evidenced by a slightly lighter, broken MT collagen stain (blue). For comparison to native tissue not exposed to an implant, histology of the sham incision experiment is included in Supplementary Data (S2). Further qualitative analysis of collagen deposition in the tissue at the implant-tissue interface by SHG showed a dimmer signal with a lower degree of orientation for the BTM sample (Fig. 3a) relative to the PTM (Fig. 3b) and NTM (Fig. 3c) samples.

3.3. Vessel Imaging and Quantification

Confocal microscopy images of αSMA- and CD31-labeled tissue sections are shown in Figure 4. Vessels within the pore network of BTM implants (Fig. 4a) were often αSMA+ and CD31+, indicating mature vessels bounded by pericytes for stabilization and regulation of the microvasculature [56]. Similar to histology results, vessels occupying the full uniform diameter of pores were observed in the BTM implants. Conversely, thin vessels were formed within the PTM implants (Fig. 4b), some of which were not αSMA+. Scatterplots of vessel sectional area within the implant samples versus distance to nearest tissue-material boundary are shown for the BTM (Fig. 4c) and PTM (Fig. 4d) [57]. Two observations were made. First, in the region near the boundary (<400 μm), both materials had vessels, however the vessel sectional area in the BTM was much larger, utilizing the open and uniform pore morphology (Fig. 4e,f) [58]. Second, at depths beyond 400 μm the PTM exhibited just a few small vessels resulting in the low vessel section area, whereas the BTM contained large vessels out to 800 μm. Not plotted is a vessel section extending from the boundary into a BTM implant growing to over 22,000 μm^2 (Fig. S3).

3.4. Macrophage Imaging and Quantification

Confocal microscopy images of tissue section slides labeled for F4/80, pan-macrophage, and CD206, “M2 pro-healing” macrophage, markers are shown in Figure 5. F4/80+ cells were scattered throughout the pore network within the BTM implant (Fig. 5a, S4a), many adhered to the implant material leaving much of the pore volume unoccupied. In contrast, F4/80+ cells, where present, occupied a large portion of the pore network within the PTM implant (Figs 5b, S4b). Also, multi-nucleated cells, which may be foreign body giant cells, were observed that tended to be F4/80+ CD206−. The number of macrophages expressing the CD206 marker is plotted as the percentage of total macrophages in implants per mouse (Fig. 5c) and in all mice per implant type (Fig. 5d). The number of CD206+ macrophages was consistently higher in BTM versus PTM implants in every mouse (Fig. 5c). Overall, the CD206 marker was present in roughly 75% compared to 46% of the observed macrophages in the BTM and PTM implants, respectively (Fig. 5d) [59,60].

4. Discussion

Biomaterials templated using bijels were implanted in mice and the tissue response to the implants was analyzed after 4 weeks. To our knowledge, this is the first *in vivo* investigation of bijel templating as a route to tissue integrating biomaterials. Our tissue analysis revealed that BTM implants were not rejected as a result of the foreign body response as full collagenous encapsulation was not present at the implant-tissue interface. In fact, evidence suggests a shift toward a more pro-healing wound response as diffuse collagen was deposited at the implant surface and within the pore network. PTM implants were also analyzed in the same animal to provide a comparison to a class of porous biomaterial used as a coating for reducing FBR to implants [17], a drainage implant for glaucoma [61], an infection resistant percutaneous device [62], and a proangiogenic tissue engineering scaffold [63]. Qualitatively, a more pronounced collagen capsule was observed at the implant-tissue interface of the PTM implants with little evidence of collagen deposition within the pore network. Immunohistochemical analysis of sectioned implants revealed a stark difference in the native tissue’s ability to utilize the pore networks of the two porous implants. Specifically, the non-constricting nature of the BTM implant allowed blood vessels to not only form and occupy the entire micro-channel diameter, “snaking” along the curved interface (Fig. 4a), but also reside deep within the implant (Fig. 4c). Pericytes bounding the vessels indicated that many of the large vessels within the BTM implant were mature in nature and would likely remain indefinitely. In contrast, the constricting windows connecting adjacent pores of the PTM implant apparently forced vessels to narrow, often leaving much of the pore volume vacant. In some cases, red blood cells were observed in single file inside narrow vessels (arrow in Fig. 4b), severely limiting blood flux in those areas of the implant. While the FBR is a very complex process involving many cell types and signals, macrophages have been identified as critical players in the progression of this immune response [48]. To probe the macrophage response to our implants, we used the established cell markers F4/80 and CD206 to label all macrophages and their pro-healing polarized subpopulation, respectively. Both porous implant types were infiltrated with macrophages (F4/80+). In the BTMs, macrophages appeared scattered throughout the pore network, while in PTM samples, they appeared to fully occupy pores only within approximately 175 μm from the tissue-implant interface. The CD206 marker indicated a difference in macrophage polarization within the two porous implant types, as the BTM case directed more of the pro-healing cells (Fig. 5c,d).

Implants for this study were synthesized from the same non-fouling material, PEGDA, using the same polymer concentration and crosslinking protocol. Even with its unique protein repulsive properties, the NTM PEGDA implants triggered the FBR as evidenced by collagen encapsulation (Fig. 2c) and F4/80+ CD206- cells at the implant-tissue interface (Fig. S5). Differences in the tissue response are therefore attributed primarily to the implant microstructure. Importantly, bijels self-assemble during spinodal decomposition, a phase separation process marked by dynamically self-similar, bicontinuous, fully percolating fluid domains [35]. The resulting energetically preferred minimum surface area interface displays negative Gaussian, zero mean, (hyperbolic or saddle) curvature. These attributes are transferred to the templated PEGDA implants resulting in pore networks that do not constrict, and do not have any “dead ends,” with a surface displaying hyperbolic curvature. In our study, the consistent pore size allowed large vessels to penetrate deep within the BTM implants (Fig. 4c). In contrast, the particle templating process relies on varying degrees of sphere fusion, which imparts pores having narrow interconnected windows (pore throats) upon template removal. The pore surfaces within this material display predominately positive Gaussian curvature. We found that the narrow windows within the pore network of PTM implants limited the size of penetrating vasculature. The constrictions may also play a role in tissue infiltration as pores were often packed with F4/80+ cells (Fig. S4). Cell migration can be stunted by the constricting nature of the pore windows [64], which may influence both macrophage polarization and vasculature formation. In contrast, cells are allowed to infiltrate the labyrinth-like pore network of BTM implants unobstructed by constrictions. Allowing macrophages and other native cells to infiltrate without obstruction may lead to significant delay or prevention of a fibrotic capsule, thereby extending the lifetime of an implantable device, such as one designed to infuse a therapeutic agent.

Feature curvature has recently been investigated in the context of cell adhesion, differentiation, and migration [65–67]. These studies have shown that the cell’s apical stress fibers orient parallel to the direction of cell migration on substrates with a zero Gaussian curvature (e.g. cylinders or flat surfaces). In contrast, on substrates that possess a negative Gaussian curvature (saddle surfaces), the stress fibers orient perpendicular to the direction of cell migration. Therefore, the predominance of negative Gaussian curvatures on the internal surfaces of BTM implants is expected to markedly influence cell-substrate interactions within these materials. Interestingly, macrophages adhered to negative Gaussian curvature surfaces (in BTM implants) were mostly polarized to the pro-healing phenotype, whereas macrophages adhered to PTM pore surfaces, having mostly positive curvatures, had a higher occurrence of the pro-inflammatory phenotype, as also observed previously by others [17]. Overall, our study introduces a new paradigm for biomaterials design based primarily on 3D morphological cues, which are created in bulk using our robust bijel templating method. Through modification of biodegradability, surface chemistry, or bioactive signals, bijel templating could provide a robust synthesis platform for next-generation biomaterials with widespread applications. Our findings also establish an important new avenue for future research. The exact mechanism by which curvature affects macrophage polarization is a formidable question of fundamental biology, and a germane research topic that warrants further investigation. The tunability of domain size afforded in bijels [32,68] enables facile and systematic variations of surface curvature in BTMs, and establishes them as the ideal platform for such studies.

5. Conclusions

We report using bijels as a template platform to create a new class of uniquely structured biomaterial implants with favorable tissue response properties. Our implants comprise a fully penetrating, non-constricting pore network and a negative Gaussian surface. PEGDA BTMs were implanted in athymic mice for four weeks. The morphological properties of the BTM implants resulted in scattered cellular infiltrate, disorganized low-density collagen deposition, increased vessel size both near the implant surface and deep within, and increased percentage of “M2 pro-healing” polarized macrophages. Overall, these factors indicate an increased integration with host tissue primarily based on the 3D morphological cues inherent to BTM implants. Future studies will need to investigate the effects of these materials in immunocompetent animals to assess if tissue responses are similar when subjected to the adaptive immune response.

Supplementary Material

Refer to Web version on PubMed Central for supplementary material.

Acknowledgements

Funding for this study was provided by the Juvenile Diabetes Research Foundation (Innovation Grant: 1-INO-2017-443-A-N), NASA Research Opportunities in Complex Fluids and Macromolecular Biophysics Program (NNX13AQ69G), and National Institutes of Health Laser Microbeam and Medical Program (P41EB015890). T.J.T. recognizes the NSF Interdisciplinary Graduate Education and Research Traineeship (IGERT) Biophotonics across Energy, Space, and Time (BEST) program for financial support and training (NSF-DGE-1144901). R.E.G. recognizes the NIH T32 Cardiovascular Applied Research and Entrepreneurship (CARE) program (HL-116270) at the Edwards Lifesciences Center for Advanced Cardiovascular Technology and UCI Graduate Division Bridge Funding for financial support and training. We thank Dr. Mark Keating for providing the MATLAB vessel tracing script and Antonio Flores for performing all surgical procedures. SEM work was performed at the UC Irvine Materials Research Institute (IMRI), using instrumentation funded in part by the National Science Foundation Center for Chemistry at the Space-Time Limit (CHE-0802913).

References

[1]. Anderson JM, Rodriguez A, Chang DT, Foreign body reaction to biomaterials, Semin. Immunol. 20 (2008) 86–100. doi:10.1016/j.smim.2007.11.004. [PubMed: 18162407]

[2]. Klopfleisch R, Jung F, The pathology of the foreign body reaction against biomaterials, J. Biomed. Mater. Res. - Part A. 105 (2017) 927–940. doi:10.1002/jbm.a.35958.

[3]. Ratner BD, Bryant SJ, Biomaterials: Where we have been and where we are going, Annu. Rev. Biomed. Eng. 6 (2004) 41–75. doi:10.1146/annurev.bioeng.6.040803.140027. [PubMed: 15255762]

[4]. Lynn AD, Blakney AK, Kyriakides TR, Bryant SJ, Temporal progression of the host response to implanted poly(ethylene glycol)-based hydrogels, J. Biomed. Mater. Res. Part A. 96A (2011) 621–631. doi:10.1002/jbm.a.33015.

[5]. Onuki Y, Bhardwaj U, Papadimitrakopoulos F, Burgess DJ, A review of the biocompatibility of implantable devices: Current challenges to overcome foreign body response, J. Diabetes Sci. Technol. 2 (2008) 1003–1015. doi:10.1177/193229680800200610. [PubMed: 19885290]

[6]. Hoffman AS, Non-fouling surface technologies, J. Biomater. Sci. Polym. Ed. 10 (1999) 1011–1014. doi:10.1163/156856299X00658. [PubMed: 10591129]

[7]. Lynn AD, Kyriakides TR, Bryant SJ, Characterization of the in vitro macrophage response and in vivo host response to poly(ethylene glycol)-based hydrogels, J. Biomed. Mater. Res. Part A. 93A (2009) 941–953. doi:10.1002/jbm.a.32595.

[8]. Nurioglu AG, Esteves ACC, de With G, Non-toxic, non-biocide-release antifouling coatings based on molecular structure design for marine applications, J. Mater. Chem. B. 3 (2015) 6547–6570. doi:10.1039/C5TB00232J. [PubMed: 32262791]

[9]. Giraldo JA, Molano RD, Rengifo HR, Fotino C, Gattás-Asfura KM, Pileggi A, Stabler CL, The impact of cell surface PEGylation and short-course immunotherapy on islet graft survival in an allogeneic murine model, Acta Biomater. 49 (2017) 272–283. doi:10.1016/j.actbio.2016.11.060. [PubMed: 27915019]

[10]. Franz S, Rammelt S, Scharnweber D, Simon JC, Immune responses to implants – A review of the implications for the design of immunomodulatory biomaterials, Biomaterials. 32 (2011) 6692–6709. doi:10.1016/j.biomaterials.2011.05.078. [PubMed: 21715002]

[11]. Leigh BL, Cheng E, Xu L, Andresen C, Hansen MR, Guymon CA, Photopolymerizable zwitterionic polymer patterns control cell adhesion and guide neural growth, Biomacromolecules. 18 (2017) 2389–2401. doi:10.1021/acs.biomac.7b00579. [PubMed: 28671816]

[12]. Tah T, Bernards MT, Nonfouling polyampholyte polymer brushes with protein conjugation capacity, Colloids Surf. B. 93 (2012) 195–201. doi:10.1016/j.colsurfb.2012.01.004.

[13]. Pham-Hua D, Padgett LE, Xue B, Anderson B, Zeiger M, Barra JM, Bethea M, Hunter CS, Kozlovskaya V, Kharlampieva E, Tse HM, Islet encapsulation with polyphenol coatings decreases pro-inflammatory chemokine synthesis and T cell trafficking, Biomaterials. 128 (2017) 19–32. doi:10.1016/j.biomaterials.2017.03.002. [PubMed: 28285194]

[14]. Kim YK, Chen EY, Liu WF, Biomolecular strategies to modulate the macrophage response to implanted materials, J. Mater. Chem. B. 4 (2016) 1600–1609. doi:10.1039/C5TB01605C. [PubMed: 32263014]

[15]. Kim YK, Que R, Wang S-W, Liu WF, Modification of biomaterials with a self-protein inhibits the macrophage response, Adv. Healthc. Mater. 3 (2014) 989–994. doi:10.1002/adhm.201300532. [PubMed: 24573988]

[16]. Stachelek SJ, Finley MJ, Alferiev IS, Wang F, Tsai RK, Eckells EC, Tomczyk N, Connolly JM, Discher DE, Eckmann DM, Levy RJ, The effect of CD47 modified polymer surfaces on inflammatory cell attachment and activation, Biomaterials. 32 (2011) 4317–4326. doi:10.1016/j.biomaterials.2011.02.053. [PubMed: 21429575]

[17]. Sussman EM, Halpin MC, Muster J, Moon RT, Ratner BD, Porous implants modulate healing and induce shifts in local macrophage polarization in the foreign body reaction, Ann. Biomed. Eng. 42 (2014) 1508–1516. doi:10.1007/s10439-013-0933-0. [PubMed: 24248559]

[18]. Luu TU, Gott SC, Woo BWK, Rao MP, Liu WF, Micro- and nanopatterned topographical cues for regulating macrophage cell shape and phenotype, ACS Appl. Mater. Interfaces. 7 (2015) 28665–28672. doi:10.1021/acsami.5b10589. [PubMed: 26605491]

[19]. Veiseh O, Dolo JC, Ma M, Vegas AJ, Tam HH, Bader AR, Li J, Langan E, Wycko J, Loo WS, Jhunjhunwala S, Chiu A, Siebert S, Tang K, Hollister-lock J, Aresta-dasilva S, Bochenek M, Mendoza-elias J, Wang Y, Qi M, Lavin DM, Chen M, Dholakia N, Thakrar R, Lacík I, Weir GC, Oberholzer J, Greiner DL, Langer R, Size- and shape-dependent foreign body immune response to materials implanted in rodents and non-human primates, Nat. Mater. 14 (2015) 643–652. doi:10.1038/NMAT4290. [PubMed: 25985456]

[20]. Salthouse TN, Some aspects of macrophage behavior at the implant interface, J. Biomed. Mater. Res. 18 (1984) 395–401. doi:10.1002/jbm.820180407. [PubMed: 6234318]

[21]. Matlaga BF, Yasenchak LP, Salthouse TN, Tissue response to implanted polymers: The significance of sample shape, J. Biomed. Mater. Res. 10 (1976) 391–397. doi:10.1002/jbm.820100308. [PubMed: 1270456]

[22]. Bryers JD, Giachelli CM, Ratner BD, Engineering biomaterials to integrate and heal: The biocompatibility paradigm shifts, Biotechnol. Bioeng. 109 (2012) 1898–1911. doi:10.1002/bit.24559. [PubMed: 22592568]

[23]. Brauker JH, Carr-brendel VE, Martinson LA, Crudele J, Johnston WD, Johnson RC, Corp BH, Park BT, Lake R, Neovascularization of synthetic membranes directed by membrane microarchitecture, J. Biomed. Mater. Res. 29 (1995) 1517–1524. doi: 10.1002/jbm.820291208. [PubMed: 8600142]

[24]. Jiang B, Waller TM, Larson JC, Appel AA, Brey EM, Fibrin-loaded porous poly(ethylene glycol) hydrogels as scaffold materials for vascularized tissue formation, Tissue Eng. Part A. 19 (2013) 224–234. doi:10.1089/ten.tea.2012.0120. [PubMed: 23003671]

[25]. Weaver JD, Headen DM, Hunckler MD, Coronel MM, Stabler CL, García AJ, Design of a vascularized synthetic poly(ethylene glycol) macroencapsulation device for islet transplantation, Biomaterials. 172 (2018) 54–65. doi:10.1016/j.biomaterials.2018.04.047. [PubMed: 29715595]

[26]. Fukano Y, Usui ML, Underwood RA, Isenhath S, Marshall AJ, Hauch KD, Ratner BD, Olerud JE, Fleckman P, Epidermal and dermal integration into sphere-templated porous poly(2-hydroxyethyl methacrylate) implants in mice, J. Biomed. Mater. Res. - Part A. 94 (2010) 1172–1186. doi:10.1002/jbm.a.32798.

[27]. Mooney DJ, Baldwin DF, Suh NP, Vacanti JP, Langer R, Novel approach to fabricate porous sponges of poly(d,l-lactic-co-glycolic acid) without the use of organic solvents, Biomaterials. 17 (1996) 1417–1422. doi:10.1016/0142-9612(96)87284-X. [PubMed: 8830969]

[28]. Bhardwaj N, Kundu SC, Electrospinning: A fascinating fiber fabrication technique, Biotechnol. Adv. 28 (2010) 325–347. doi:10.1016/j.biotechadv.2010.01.004. [PubMed: 20100560]

[29]. Welzel PB, Grimmer M, Renneberg C, Naujox L, Zschoche S, Freudenberg U, Werner C, Macroporous starPEG-heparin cryogels, Biomacromolecules. 13 (2012) 2349–2358. doi:10.1021/bm300605s. [PubMed: 22758219]

[30]. Nalawade AC, V Ghorpade R, Shadbar S, Qureshi MS, Chavan NN, Khan AA, Ponrathnam S, Inverse high internal phase emulsion polymerization (i-HIPE) of GMMA, HEMA and GDMA for the preparation of superporous hydrogels as a tissue engineering scaffold, J. Mater. Chem. B. 4 (2016) 450–460. doi:10.1039/C5TB01873K. [PubMed: 32263209]

[31]. Stratford K, Adhikari R, Pagonabarraga I, Desplat J-C, Cates ME, Colloidal jamming at interfaces: A route to fluid-bicontinuous gels, Science. 309 (2005) 2198–2201. doi:10.1126/science.1116589. [PubMed: 16195456]

[32]. Herzig EM, White KA, Schofield AB, Poon WCK, Clegg PS, Bicontinuous emulsions stabilized solely by colloidal particles, Nat. Mater. 6 (2007) 966–971. doi:10.1038/nmat2055. [PubMed: 17982465]

[33]. Lee MN, Thijssen JHJ, Witt JA, Clegg PS, Mohraz A, Making a robust interfacial scaffold: Bijel rheology and its link to processability, Adv. Funct. Mater. 23 (2013) 417–423. doi:10.1002/adfm.201201090.

[34]. Imperiali L, Clasen C, Fransaer J, Macosko CW, Vermant J, A simple route towards graphene oxide frameworks, Mater. Horizons. 1 (2014) 139–145. doi:10.1039/c3mh00047h.

[35]. Reeves M, Stratford K, Thijssen JHJ, Quantitative morphological characterization of bicontinuous Pickering emulsions via interfacial curvatures, Soft Matter. 12 (2016) 4082–4092. doi:10.1039/C5SM03102H. [PubMed: 27035101]

[36]. Lee MN, Mohraz A, Bicontinuous macroporous materials from bijel templates, Adv. Mater. 22 (2010) 4836–4841. doi:10.1002/adma.201001696. [PubMed: 20862712]

[37]. Witt JA, Mumm DR, Mohraz A, Microstructural tunability of co-continuous bijel-derived electrodes to provide high energy and power densities, J. Mater. Chem. A. 4 (2016) 1000–1007. doi:10.1039/C5TA06260H.

[38]. Lee MN, Santiago-Cordoba MA, Hamilton CE, Subbaiyan NK, Duque JG, Obrey KAD, Developing monolithic nanoporous gold with hierarchical bicontinuity using colloidal bijels, J. Phys. Chem. Lett. 5 (2014) 809–812. doi:10.1021/jz5001962. [PubMed: 26274071]

[39]. Lee MN, Mohraz A, Hierarchically porous silver monoliths from colloidal bicontinuous interfacially jammed emulsion gels, J. Am. Chem. Soc. 133 (2011) 6945–6947. doi:10.1021/ja201650z. [PubMed: 21452833]

[40]. Thorson TJ, Botvinick EL, Mohraz A, Composite bijel-templated hydrogels for cell delivery, ACS Biomater. Sci. Eng. 4 (2018) 587–594. doi:10.1021/acsbiomaterials.7b00809. [PubMed: 30555892]

[41]. Haase MF, Jeon H, Hough N, Kim JH, Stebe KJ, Lee D, Multifunctional nanocomposite hollow fiber membranes by solvent transfer induced phase separation, Nat. Commun. 8 (2017) 1234. doi:10.1038/s41467-017-01409-3. [PubMed: 29089498]

[42]. Di Vitantonio G, Wang T, Haase MF, Stebe KJ, Lee D, Robust bijels for reactive separation via silica-reinforced nanoparticle layers, ACS Nano. 13 (2019) 26–31. doi:10.1021/acsnano.8b05718. [PubMed: 30525442]

[43]. Van Blaaderen A, Vrij A, Synthesis and characterization of colloidal dispersions of fluorescent, monodisperse silica spheres, Langmuir. 8 (1992) 2921–2931. doi:10.1021/la00048a013.

[44]. Huang C, Forth J, Wang W, Hong K, Smith GS, Helms BA, Russell TP, Bicontinuous structured liquids with sub-micrometre domains using nanoparticle surfactants, Nat. Nanotechnol. 12 (2017) 1060–1063. doi:10.1038/nnano.2017.182. [PubMed: 28945242]

[45]. Binks BP, Particles as surfactants—similarities and differences, Curr. Opin. Colloid Interface Sci. 7 (2002) 21–41. doi:10.1016/S1359-0294(02)00008-0.

[46]. White KA, Schofield AB, Wormald P, Tavacoli JW, Binks BP, Clegg PS, Inversion of particle-stabilized emulsions of partially miscible liquids by mild drying of modified silica particles, J. Colloid Interface Sci. 359 (2011) 126–135. doi:10.1016/j.jcis.2011.03.074. [PubMed: 21507417]

[47]. Chen X, Xue Z, Yao Y, Wang W, Zhu F, Hong C, Oxidation degradation of rhodamine B in aqueous by UV/S 2O 82- treatment system, Int. J. Photoenergy. 2012 (2012). doi:10.1155/2012/754691.

[48]. Doloff JC, Veiseh O, Vegas AJ, Tam HH, Farah S, Ma M, Li J, Bader A, Chiu A, Sadraei A, Aresta-Dasilva S, Griffin M, Jhunjhunwala S, Webber M, Siebert S, Tang K, Chen M, Langan E, Dholokia N, Thakrar R, Qi M, Oberholzer J, Greiner DL, Langer R, Anderson DG, Colony stimulating factor-1 receptor is a central component of the foreign body response to biomaterial implants in rodents and non-human primates, Nat. Mater. 16 (2017) 671–680. doi:10.1038/nmat4866. [PubMed: 28319612]

[49]. Schindelin J, Arganda-Carreras I, Frise E, Kaynig V, Longair M, Pietzsch T, Preibisch S, Rueden C, Saalfeld S, Schmid B, Tinevez JY, White DJ, Hartenstein V, Eliceiri K, Tomancak P, Cardona A, Fiji: An open-source platform for biological-image analysis, Nat. Methods. 9 (2012) 676–682. doi:10.1038/nmeth.2019. [PubMed: 22743772]

[50]. Preibisch S, Saalfeld S, Tomancak P, Globally optimal stitching of tiled 3D microscopic image acquisitions, Bioinformatics. 25 (2009) 1463–1465. doi:10.1093/bioinformatics/btp184. [PubMed: 19346324]

[51]. Gurlin RE, Keating MT, Li S, Lakey JR, de Feraudy S, Shergill BS, Botvinick EL, Vascularization and innervation of slits within polydimethylsiloxane sheets in the subcutaneous space of athymic nude mice, J. Tissue Eng. 8 (2017). doi:10.1177/2041731417691645.

[52]. Lucas T, Waisman A, Ranjan R, Roes J, Krieg T, Muller W, Roers A, Eming SA, Differential roles of macrophages in diverse phases of skin repair, J. Immunol. 184 (2010) 3964–3977. doi:10.4049/jimmunol.0903356. [PubMed: 20176743]

[53]. Yu T, Wang W, Nassiri S, Kwan T, Dang C, Liu W, Spiller KL, Temporal and spatial distribution of macrophage phenotype markers in the foreign body response to glutaraldehyde-crosslinked gelatin hydrogels, J. Biomater. Sci. Polym. Ed. 27 (2016) 721–742. doi:10.1080/09205063.2016.1155881. [PubMed: 26902292]

[54]. Dollinger C, Ndreu-Halili A, Uka A, Singh S, Sadam H, Neuman T, Rabineau M, Lavalle P, Dokmeci MR, Khademhosseini A, Ghaemmaghami AM, Vrana NE, Controlling incoming macrophages to implants: Responsiveness of macrophages to gelatin micropatterns under M1/M2 phenotype defining biochemical stimulations, Adv. Biosyst. 1 (2017) 1700041. doi:10.1002/adbi.201700041.

[55]. Edelstein AD, Tsuchida MA, Amodaj N, Pinkard H, Vale RD, Stuurman N, Advanced methods of microscope control using μManager software, J. Biol. Methods. 1 (2014) 10. doi:10.14440/jbm.2014.36.

[56]. Armulik A, Abramsson A, Betsholtz C, Endothelial/pericyte interactions, Circ. Res. 97 (2005) 512–523. doi:10.1161/01.RES.0000182903.16652.d7. [PubMed: 16166562]

[dataset][57]. Thorson T, Gurlin R, Botvinick E, Mohraz A, Raw vessel quantification data for 28-day bijel-templated implant study in nude mice, Mendeley Data, V2, 2019 10.17632/bms5txwp2h.2.

[dataset][58]. Thorson T, Gurlin R, Botvinick E, Mohraz A, Processed vessel quantification data for 28-day bijel-templated implant study in nude mice, Mendeley Data, V5, 2019 10.17632/hgssh35z5k.5.

[dataset][59]. Thorson T, Gurlin R, Botvinick E, Mohraz A, Raw macrophage quantification data for 28-day bijel-templated implant study in nude mice, Mendeley Data, V2, 2019 10.17632/5f38n5xfjx.2.

[dataset][60]. Thorson T, Gurlin R, Botvinick E, Mohraz A, Processed macrophage quantification data for 28-day bijel-templated implant study in nude mice, Mendeley Data, V2, 2019 10.17632/n9bcksssfj.2.

[61]. Pourjavan S, Collignon NJM, De Groot V, Eiferman RA, Marshall AJ, Roy CJ, STARfloTM: A Suprachoroidal Drainage Implant Made from STAR® Biomaterial, in: Samples JR, Ahmed IIK (Eds.), Surg. Innov. Glaucoma, Springer New York, New York, NY, 2014: pp. 235–251. doi:10.1007/978-1-4614-8348-9_22.

[62]. Isenhath SN, Fukano Y, Usui ML, Underwood RA, Irvin CA, Marshall AJ, Hauch KD, Ratner BD, Fleckman P, Olerud JE, A mouse model to evaluate the interface between skin and a percutaneous device, J. Biomed. Mater. Res. Part A. 83A (2007) 915–922. doi:10.1002/jbm.a.31391.

[63]. Madden LR, Mortisen DJ, Sussman EM, Dupras SK, Fugate JA, Cuy JL, Hauch KD, Laflamme MA, Murry CE, Ratner BD, Proangiogenic scaffolds as functional templates for cardiac tissue engineering., Proc. Natl. Acad. Sci. U. S. A. 107 (2010) 15211–6. doi:10.1073/pnas.1006442107. [PubMed: 20696917]

[64]. Stachowiak AN, Irvine DJ, Inverse opal hydrogel-collagen composite scaffolds as a supportive microenvironment for immune cell migration, J. Biomed. Mater. Res. Part A. 85A (2008) 815–828. doi:10.1002/jbm.a.31661.

[65]. Werner M, Blanquer SBG, Haimi SP, Korus G, Dunlop JWC, Duda GN, Grijpma DW, Petersen A, Surface curvature differentially regulates stem cell migration and differentiation via altered attachment morphology and nuclear deformation, Adv. Sci. 4 (2017) 1–11. doi:10.1002/advs.201600347.

[66]. Bade ND, Kamien RD, Assoian RK, Stebe KJ, Curvature and Rho activation differentially control the alignment of cells and stress fibers, Sci. Adv. 3 (2017) 1–9. doi:10.1126/sciadv.1700150.

[67]. Bade ND, Xu T, Kamien RD, Assoian RK, Stebe KJ, Gaussian curvature directs stress fiber orientation and cell migration, Biophys. J. 114 (2018) 1467–1476. doi:10.1016/j.bpj.2018.01.039. [PubMed: 29590603]

[68]. Witt JA, Mumm DR, Mohraz A, Bijel reinforcement by droplet bridging: a route to bicontinuous materials with large domains, Soft Matter. 9 (2013) 6773–6780. doi:10.1039/c3sm00130j.

Statement of Significance

All implanted biomaterials are subject to the foreign body response (FBR) which can have a detrimental effect on their efficacy. Altering the surface chemistry can decrease the FBR by limiting the amount of proteins adsorbed to the implant. This effect can be enhanced by including pores in the biomaterial to allow new tissue growth as the implant becomes integrated in the body. Here, we introduce a new class of self-assembled biomaterials comprising a fully penetrating, non-constricting pore phase with hyperbolic (saddle) surfaces for enhanced tissue integration. These unique morphological characteristics result in dense blood vessel formation and favorable tissue response properties demonstrated in a four-week implantation study.

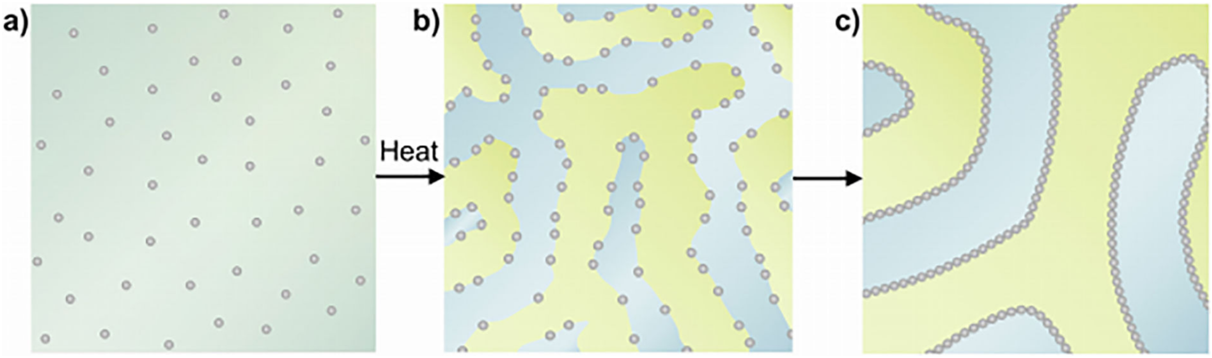

Fig. 1.

Bijel formation schematic. (a) Particles are dispersed in a critical composition of water and 2,6-lutidine (mole fraction of 2,6-luitidine, $x_{lut} = 0.064$). (b) Heating above the lower critical solution temperature (34.1 °C) prompts spinodal decomposition and particle adsorption at the coarsening interface. (c) The system arrests as the interface becomes completely occupied by particles.

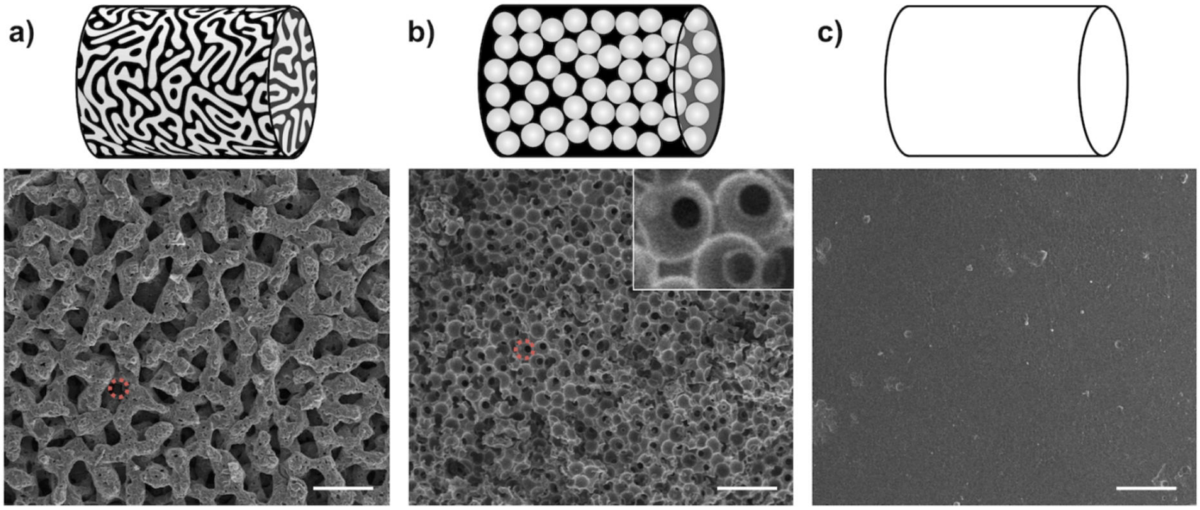

Figure 2.

Template materials and scanning electron microscopy micrographs of polymer implants. Pictured are (a) BTM, (b) PTM, and (c) NTM polyethylene glycol diacrylate implants. Scale bar, 100 µm. Superimposed red circle diameter in panels (a) and (b), 32 µm.

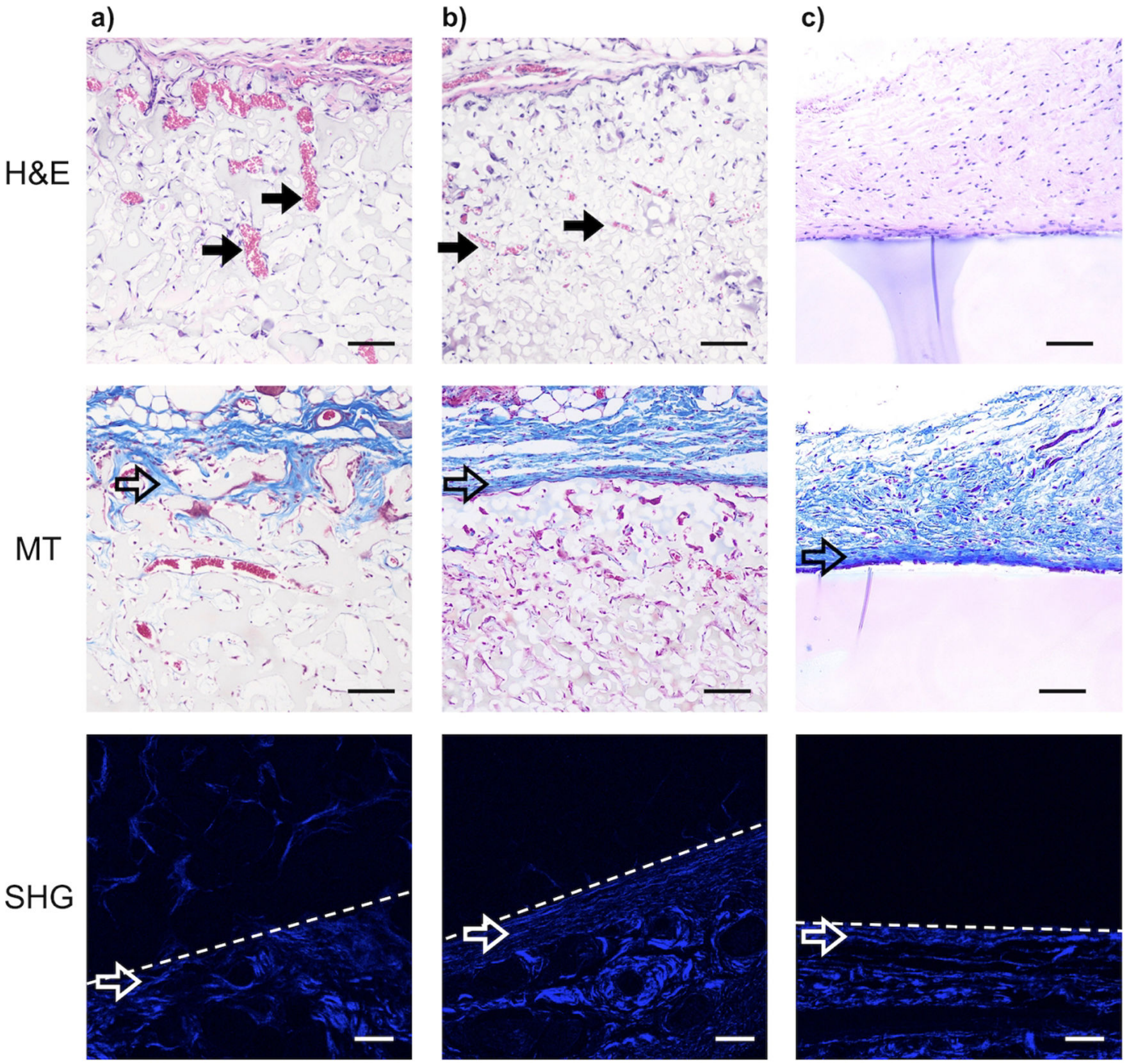

Figure 3.

Histology and second harmonic generation (SHG) of BTM (a), PTM (b), and NTM (c) implants. Histology sections stained with hematoxylin and eosin (H&E) shown in row 1 and Masson’s trichrome (MT) shown in row 2. Scale bar, 100 μm. Sections imaged using second harmonic generation (SHG) shown in row 3. Filled arrows and open arrows denote blood vessels and collagen networks, respectively. White dashed line denotes tissue-implant boundary with implant oriented on top. Scale bar, 50 μm.

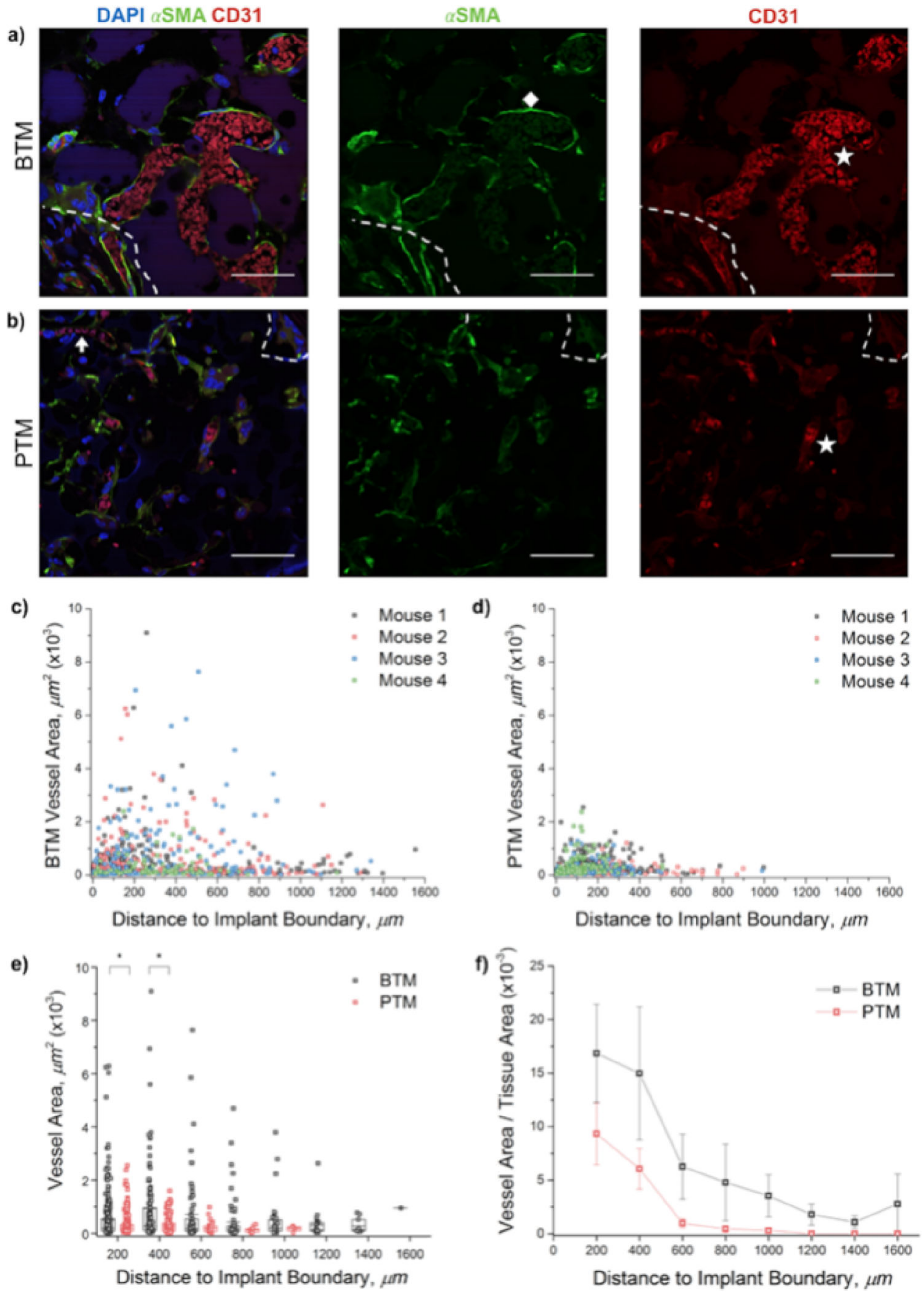

Figure 4.

Vessel immunohistochemistry and quantification. Shown are CD31 (red), αSMA (green), and DAPI (blue) labeling in BTM (a) and PTM (b) implants. DAPI counterstaining shown in blue. Dashed lines denote implant boundary, an arrow denotes a thin vessel extending through pore-pore windows, a diamond denotes a αSMA+ cell, and stars denote CD31+ cells. Scale bar, 50 μm. Vessel area versus distance to nearest implant boundary in BTM (c) and PTM (d) implants. Vessel area versus distance to boundary (200 μm bin width), plotted for all vessels across all mice (e), and as mean ± standard error of the mean of total vessel area per mouse (n=4) (f). $*p < 0.05$

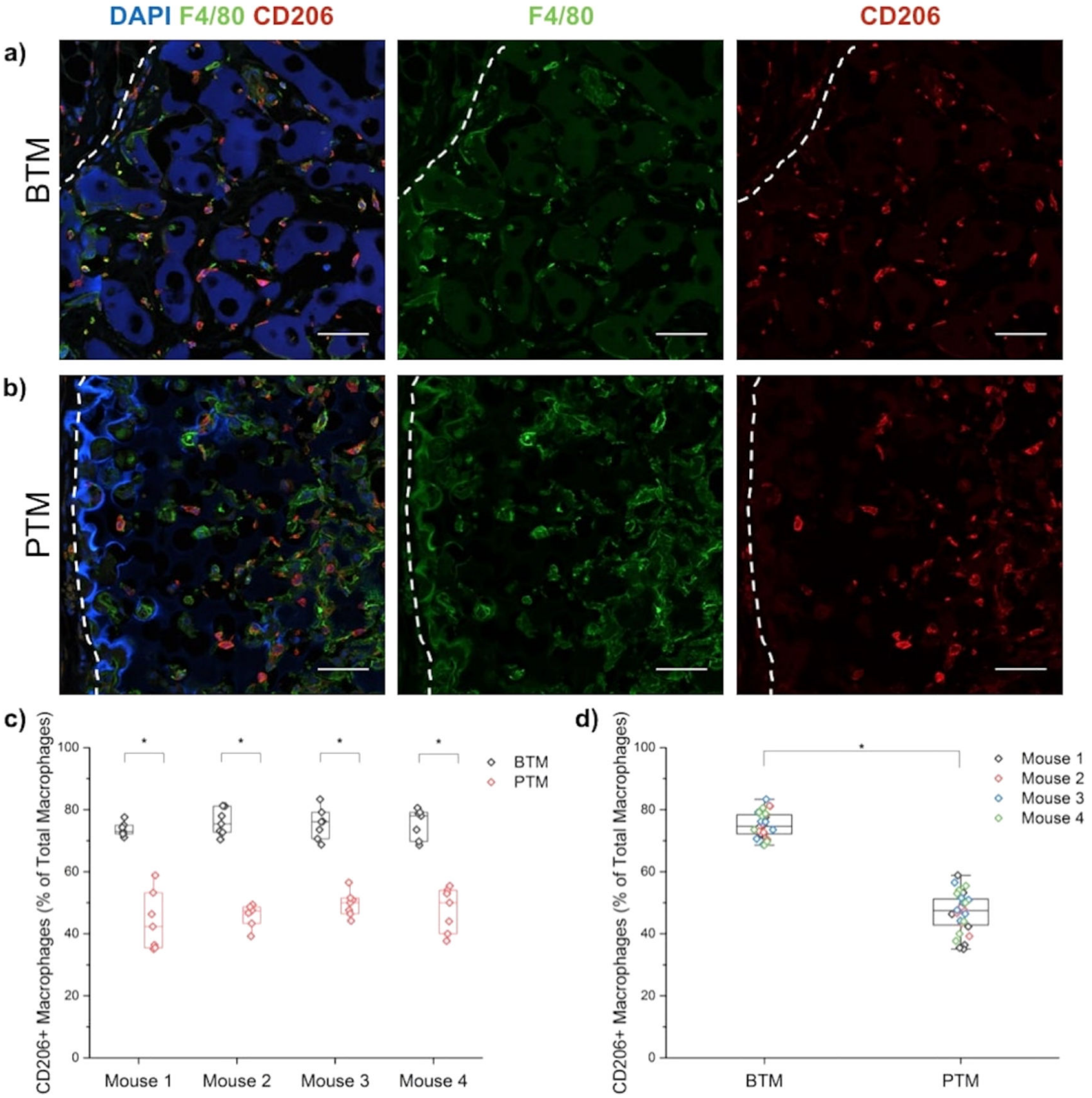

Figure 5.

Macrophage immunohistochemistry and quantification. Shown are F4/80 (green) and CD206 (red) labeling in BTM (a) and PTM (b) implants. DAPI counterstaining shown in blue. Dashed lines denote implant boundary. Scale bar, 50 μm. Percent CD206+ cells relative to total F4/80+ cells for both implant types in each mouse (c-d). $*p < 0.05$.